AMERICAN SOCIETY FOR MICROBIOLOGY | Applied and Environmental Microbiology®

BIOTECHNOLOGY

# High-Throughput Microfluidic Sorting of Live Magnetotactic Bacteria

**Andy Tay,[a,b] Daniel Pfeiffer,[c] Kathryn Rowe,[d] Aaron Tannenbaum,[d] Felix Popp,[c] Robert Strangeway,[d] Dirk Schüler,[c] Dino Di Carlo[a,e,f,g]**

[a]Department of Bioengineering, University of California, Los Angeles, Los Angeles, California, USA
[b]Department of Biomedical Engineering, National University of Singapore, Singapore
[c]Department of Microbiology, University of Bayreuth, Bayreuth, Germany
[d]Institute of Geophysics and Planetary Physics, University of California, Los Angeles, Los Angeles, California, USA
[e]California NanoSystems Institute, University of California, Los Angeles, Los Angeles, California, USA
[f]Jonsson Comprehensive Cancer Center, University of California, Los Angeles, Los Angeles, California, USA
[g]Department of Mechanical and Aerospace Engineering, University of California, Los Angeles, Los Angeles, California, USA

**ABSTRACT** Magnetic nanoparticles (MNPs) are useful for many biomedical applications, but it is challenging to synthetically produce them in large numbers with uniform properties and surface functionalization. Magnetotactic bacteria (MTB) produce magnetosomes with homogenous sizes, shapes, and magnetic properties. Consequently, there is interest in using MTB as biological factories for MNP production. Nonetheless, MTB can only be grown to low yields, and wild-type strains produce low numbers of MNPs/bacterium. There are also limited technologies to facilitate the selection of MTB with different magnetic contents, such as MTB with compromised and enhanced biomineralization ability. Here, we describe a magnetic microfluidic platform combined with transient cold/alkaline treatment to temporarily reduce the rapid flagellar motion of MTB without compromising their long-term proliferation and biomineralization ability for separating MTB on the basis of their magnetic contents. This strategy enables live MTB to be enriched, which, to the best of our knowledge, has not been achieved with another previously described magnetic microfluidic device that makes use of ferrofluid and heat. Our device also facilitates the high-throughput (25,000 cells/min) separation of wild-type *Magnetospirillum gryphiswaldense* (MSR-1) from nonmagnetic Δ*mamAB* MSR-1 mutants with a sensitivity of up to 80% and isolation purity of up to 95%, as confirmed with a gold-standard fluorescent-activated cell sorter (FACS) technique. This offers a 25-fold higher throughput than other previously described magnetic microfluidic platforms (1,000 cells/min). The device can also be used to isolate *Magnetospirillum magneticum* (AMB-1) mutants with different ranges of magnetosome numbers with efficiencies close to theoretical estimates. We believe this technology will facilitate the magnetic characterization of genetically engineered MTB for a variety of applications, including using MTB for large-scale, controlled MNP production.

**IMPORTANCE** Our magnetic microfluidic technology can greatly facilitate biological applications with magnetotactic bacteria, from selection and screening to analysis. This technology will be of interest to microbiologists, chemists, and bioengineers who are interested in the biomineralization and selection of magnetotactic bacteria (MTB) for applications such as directed evolution and magnetogenetics.

**KEYWORDS** magnetotactic bacteria, microfluidic, enrichment, magnetic nanoparticles

**Received** 29 May 2018 **Accepted** 23 June 2018

**Accepted manuscript posted online** 29 June 2018

**Citation** Tay A, Pfeiffer D, Rowe K, Tannenbaum A, Popp F, Strangeway R, Schüler D, Di Carlo D. 2018. High-throughput microfluidic sorting of live magnetotactic bacteria. Appl Environ Microbiol 84:e01308-18. https://doi.org/10.1128/AEM.01308-18.

**Editor** Robert M. Kelly, North Carolina State University



Address correspondence to Dino Di Carlo, dicarlo@ucla.edu.

Magnetic nanoparticles (MNPs) are employed in diverse biomedical applications, including cancer hyperthermia and neural stimulation (1, 2). One of the most widely used materials for MNPs is chemically synthesized iron oxide. Ideally, MNPs should have (i) uniform sizes with a low polydispersity index for consistent results, (ii) high stability in aqueous solutions to reduce aggregation, (iii) high magnetic and thermal stability and low cytotoxicity for interfacing with biological entities, and (iv) high flexibility for surface chemistry to enable drug and biological polymer conjugation (3). Although advances in nanotechnology such as microfluidic-assisted nanoparticle synthesis have made some of these properties possible (4), a successful result usually comes with a compromise on the manufacturing costs and time, which can be prohibitive for industrial production and the research/medical use of MNPs (5). Lastly, the large-scale production of MNPs is still a challenge due to the stringent requirements for a narrow size distribution, though there has been recent progress in the chemical synthesis of MNPs with uniform properties using nontoxic precursors with gram-scale production capabilities (6, 7).

Making use of a unique biomineralization process, magnetotactic bacteria (MTB) can assemble and precipitate linear chains of magnetite [$Fe(II)Fe(III)_2O_4$] NPs with different shapes (spherical, bullet, etc.) and sizes (35 to 120 nm) bound in lipid membranes known as magnetosomes unique to the strains (8). Magnetosomes produced by MTB have homogeneous sizes (narrow polydispersity index) and crystallography (ferrimagnetic), possess high thermal stability, and have low aggregation, and their lipid coating enables simple surface chemistry or the construction of fusions to proteins that localize to the magnetosome membrane for biomedical applications (9). Consequently, there is growing interest in employing MTB as biological factories for a large-scale controlled synthesis of magnetosomes. There are ongoing efforts to understand the roles of different genes in the magnetosome gene island as well as accessory genes in order to execute targeted genetic manipulations for the generation of MTB overproducers (10, 11). Alternatively, directed evolution can be used to enrich mutant MTB overproducers (12).

Current tools for screening MTB on the basis of the quantity of the magnetic material per cell are limited. The available tools used are electron microscopy (EM), $C_{mag}$ (i.e., the magnetic response determined by light scattering assays), and color inspection of the bacterial colonies (see Fig. S1 in the supplemental material) (13). These methods are slow, subjective, and labor intensive despite providing only semiquantitative information (see Table S1). Myklatun et al. recently designed a microfluidic platform filled with ferrofluid for the isolation of MTB (14). However, with the combined (MTB and buffer) flow rate of 0.6 $\mu$l/min, the throughput of the system is extremely low, i.e., 1,000 cells/min (14). The use of ferrofluid and long sorting time due to the low throughput can also affect the long-term growth, viability, or magnetosome production of MTB, but these effects were not further characterized by Myklatun and colleagues.

Microfluidic flow has been exploited for cell separation based on cellular properties such as size, deformability, surface antigen expression, and magnetic content (15). Magnetic microfluidic devices have also been designed to isolate cells with internalized magnetic particles for applications such as detection of *Escherichia coli* (16) and HIV (17). The microdimensions of microfluidic channels enable steep spatial gradients in magnetic fields to be established locally to generate significant magnetic forces. Capitalizing on previous work, we designed a magnetic microfluidic platform to deflect the motion of MTB by their numbers of ferrimagnetic magnetosomes as they flow through the microchannels.

However, unlike what has been demonstrated when using similar microfluidic platforms to separate eukaryotic cells, MTB are highly motile. We observed that the bacterial flagellar motion can overcome magnetic forces, leading to false positives (reduced purity) and negatives (reduced yield). To overcome rapid bacterial flagellar motion, we implemented a strategy where we transiently treated *Magnetospirillum gryphiswaldense* wild-type (WT) strain MSR-1 (18) and MSR-1 Δ*mamAB* (19) that does

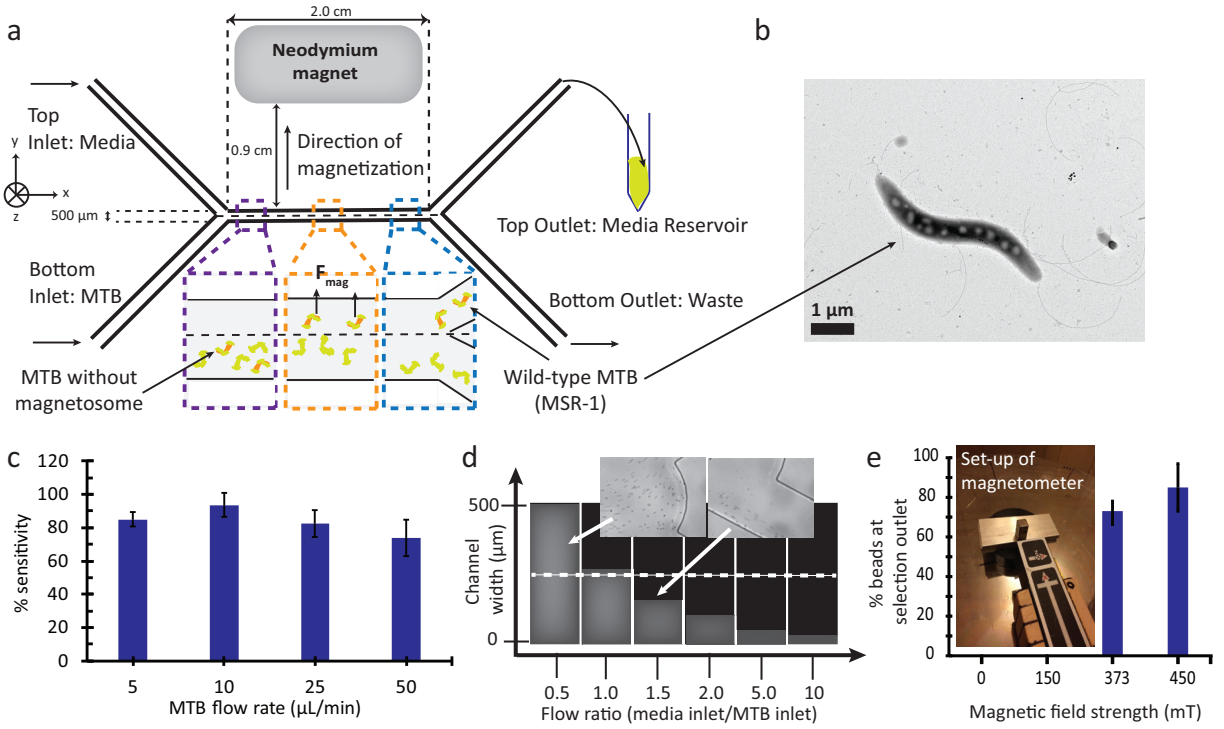


**FIG 1** Optimizing parameters for microchannel flow. (a) Design of the microfluidic device for magnetic deflection. (b) Representative micrographs of the MSR-1 wild type. The average length of MSR-1 is approximately 3 $\mu$m. (c) Percent sensitivity in isolating 3-$\mu$m beads from waste outlet was highest at MTB inlet flow rate of 10 $\mu$l/min with flow ratio of 1:1. (d) Focusing behaviors of 3-$\mu$m beads at different flow ratios. A minimum flow ratio (top buffer inlet/bottom MTB inlet) of 1.5 is needed to completely focus all the nonmagnetic beads into the waste outlet. The gray-colored areas represent the widths filled by the 3-$\mu$m beads. Insets show the focusing widths of the 3-$\mu$m beads. (e) Deflection of 1-$\mu$m magnetic beads at different magnetic field strengths. A magnetic field strength of 373 mT is sufficient to deflect ~70% of 1-$\mu$m magnetic beads. Magnetic field strengths lower than 373 mT did not deflect any detectable magnetic beads. Inset shows the setup of magnetometer measurements. Bar charts indicate mean values, and error bars are standard deviations from 3 independent experiments.

not have magnetosomes with cold/alkaline medium (10°C, pH 8.5), which did not affect their growth and magnetosome production after microfluidic isolation.

We achieved a live high-throughput (1,000 cells/$\mu$l $\times$ 25 $\mu$l/min = 25,000 cells/min) enrichment and estimation of magnetic content of *Magnetospirillum gryphiswaldense* (MSR-1) with up to 80% sensitivity and 95% isolation purity. The device can also be used to isolate *Magnetospirillum magneticum* strain AMB-1 mutants with different ranges of magnetosome numbers. This demonstration highlights the utility of our device for microbiologists investigating the impact of different genes on MTB biomineralization ability. We believe our microfluidic technology can greatly facilitate biological applications, such as mutant selection after genetic engineering.

## RESULTS

**Design of magnetic microfluidic device.** The magnetic microfluidic device consists of 2 inlets, namely, a top inlet for medium and a bottom inlet for MTB suspension, and 2 outlets, i.e., for selection (top) and waste (bottom) (Fig. 1a). A neodymium magnet is placed adjacent to the microchannel to generate a local magnetic field. An incision approximately the dimension of the magnet (2 cm) is made ~0.9 cm away from the microchannel to hold the magnet firmly in place. MTB flow through the bottom inlet and experience different magnitudes of magnetic forces on the basis of their magnetic contents, which determines whether they exit through the selection or waste outlet. The cross-stream migration of MTB is determined by the balance between Stokes drag and magnetic forces (see Table S2 in the supplemental material). MTB having more magnetosomes experienced greater magnetic forces, which increased their terminal velocity (*y* axis) for crossing the stream.

To use the Stokes drag equation, we assumed that the bacterium is spherical in shape. Although MTB are cylindrical/helical in shape, the Stokes drag around a nonspherical object can be modeled with a shape factor determined experimentally by Johnson (described in reference 20). For the case of the cylindrically shaped bacterium, the shape factor is 0.75 and can be calculated by substituting values into the equations outlined in reference 20. This shape factor value makes spherical particle a good approximation for the flow characterization of cylinder-shaped MTB (see calculation at Table S2). The cylindrical/rod-shaped approximation of MTB has also been adopted by others in the MTB field (21).

**Optimizing flow conditions with particles.** To understand the initial streamlines occupied by MTB under conditions of flow in microchannels, we first characterized the motion of 3-$\mu$m nonmagnetic spherical beads, which are about the average length of MTB (Fig. 1b). This process is also useful to pinch the bottom stream, as the positions of the MTB cells along the *z*-axis parabolic velocity profiles affect their transit time for crossing the stream (22). As expected on the basis of the conservation of mass, with a higher flow ratio between the top buffer and bottom particle inlets, the particles focused closer to the bottom channel wall.

We first characterized the sensitivity of the microfluidic device in isolating 3-$\mu$m nonmagnetic spherical beads at different MTB inlet flow rates and at a flow ratio (top medium inlet/bottom MTB inlet) of 1:1. Note that the sensitivity is calculated by quantifying the percentage of 3-$\mu$m beads isolated at the waste outlet with a flow cytometer. At a low flow rate of 5 $\mu$l/min, we observed flow instability and a significant time lag before flow stabilization. We reasoned that this would reduce the user friendliness of the tool. Therefore, we further characterized the sensitivity at flow rates of 10, 25, and 50 $\mu$l/min and found the highest isolation sensitivity at an MTB inlet flow rate of 10 $\mu$l/min (Fig. 1c).

We next observed the particle-focusing behavior at a flow ratio of 0.5 to 10 (top medium inlet/bottom MTB inlet) with the optimized MTB inlet flow rate of 10 $\mu$l/min. Figure 1d shows the tighter focusing of the beads at the bottom channel wall as the flow ratio increased. We found that a flow ratio of 1.5 (medium inlet/MTB inlet) provided focusing sufficient to minimize the number of low-magnetic-content MTB being collected at the selection outlet. This helped to minimize false positives to increase the isolation purity at the selection outlet.

We then measured the magnetic fields of our neodymium magnets. We made use of a highly sensitive magnetometer, typically used to measure the magnetic fields of planetary systems (insert in Fig. 1e). The obtained readings match the theoretical calculations based on parameters from the manufacturer (see Fig. S2). We then characterized the deflection of 1-$\mu$m magnetic beads under conditions of different magnetic field strengths of 0 to 450 mT at the optimized MTB inlet flow rate of 10 $\mu$l/min and flow ratio of 1.5. As the distance between the magnet and microchannel was kept constant, a stronger magnet provided a steeper field gradient to generate stronger upward forces (see equation 1 for Table S2). The average number of magnetosomes/MSR-1 bacterium was ~20 (23). On the basis of the magnetic properties of the magnetosomes, a chain of 20 magnetosomes was expected to experience a similar magnetic force as a 1-$\mu$m magnetic bead due to their similar magnetic volumes (see Table S3) (23). In calculating the magnetic volumes of magnetosomes, we assumed the shape to be spherical, which is typically used in the MTB field (24). Neodymium magnets with magnetic field strengths of 373 mT (Fig. S2) and 450 mT deflected ~70% and ~80% of 1-$\mu$m magnetic beads (1,000 beads/$\mu$l) into the selection outlet, respectively (Fig. 1e). This characterization enabled us to establish the threshold magnetic field/force to isolate the MSR-1 wild type, i.e., those with ~20 magnetosomes/bacterium (Fig. 1b), from the nonmagnetic Δ*mamAB* mutant.

**Cold/alkaline treatment to minimize flagellar motion.** We observed that at the optimized flow rate of 10 $\mu$l/min for the bottom MTB inlet, the bacterial flagellar motion overcame the magnetic forces, thus reducing the isolation purity and yield. We hence

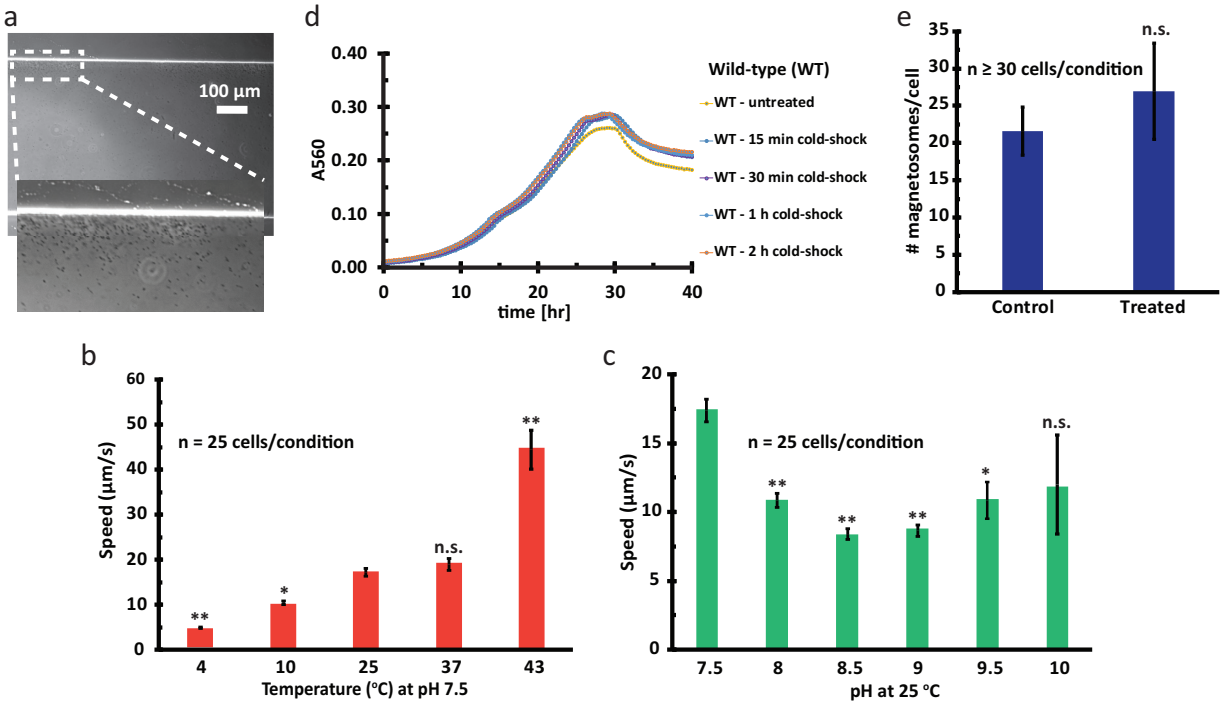


**FIG 2** Cold/alkaline treatment as a strategy to minimize flagellar motion. (a) MSR-1 in microfluidic chambers showing clustering near microchannel walls where the oxygen gradient was steeper. (b) Normalized root mean square (RMS) speed of MSR-1 (to 25°C, pH 7.5) at different temperatures; $n = 25$ cells for each condition. (c) Normalized RMS speed of MSR-1 (to 25°C, pH 7.5) at different pHs; $n = 25$ cells for each condition. Bar charts indicate mean values and error bars are standard deviations from 25 cells/condition. No significant difference in growth rates (d) or magnetosome number per cell ($n \geq 30$ cell/condition) (e) between MSR-1 control and MSR-1 treated with cold/alkaline medium followed by 3 days of culturing in normal medium. *, $P < 0.05$; **, $P < 0.001$ relative to condition at 25°C and pH 7.5; n.s., nonsignificant. Note that MSR-1 cells were cultivated at 30°C but normalization was performed at 25°C and pH 7.5 as microfluidic cell sorting was performed at this temperature.

evaluated motility under different conditions and sought a convenient strategy to modify the operation environment to minimize flagellar movements. While it is also possible to perform genetic knockout of the *flaA* gene (18) to minimize flagellar motion, this strategy is inconvenient, requires time for mutant generation and screening, and would not be applicable for newly discovered MTB strains that cannot be cultured easily.

MTB are oxygen sensitive and their swimming behaviors are affected by oxygen concentrations (25). As polydimethylsiloxane (PDMS) is permeable to oxygen, we found that under a stagnant flow condition, MSR-1 tended to cluster near the walls of the microchannel (Fig. 2a; see also Video S1). There are several reports in the literature documenting MTB mobility at different temperatures and pHs but, unfortunately, without proper oxygen level and gradient control (25–27). As our purpose was to identify the conditions that best minimized flagellar motion, we need to emphasize that the values obtained here are specific to our microfluidic chamber with the following dimensions: length, 2 cm; width, 500 $\mu$m; height, 23 $\mu$m. The mean swimming speed in our case was approximately 17.5 $\mu$m/s for MSR-1 at 25°C and pH 7, similar to that (20 $\mu$m/s) reported by Lefèvre et al. (25).

We first tracked the motion of MSR-1 cells at 4°C, 10°C, 25°C, 37°C, and 43°C and found that as the temperature increased, the normalized root mean square (RMS) speed increased, possibly due to greater bacterial metabolic rates (Fig. 2b). We also tracked the bacterial swimming speed from pH 7.5 (their typical growth medium condition) to pH 10 with 0.5 step increments. Consistent with the knowledge that flagellar mobility is powered by the proton gradient, we observed that as the pH became less acidic (i.e., fewer available protons), the normalized RMS speed decreased (Fig. 2c). Interestingly, at pH 9.5 and 10, the trend reversed, which we hypothesize might be due to the activation of stress responses in MSR-1 (28).

Next, we assessed the growth and number of magnetosomes per cell for wild-type MSR-1 cells transiently treated with cold/alkaline medium. The treatment time was determined on the basis of the maximum time that MSR-1 were under these conditions during microfluidic flow, i.e., 45 min (see Table S4). Recently, Myklatun et al. reported the use of a magnetic microfluidic platform to isolate MSR-1 (14). In their work, they immobilized MSR-1 by treatment with 75°C medium for 15 min, but they did not demonstrate subsequent culture of MSR-1. This is a concern, as a high temperature is expected to significantly reduce cell viability compared to that with a low temperature (10°C), which primarily reduces metabolic rates. As expected, cold/alkaline treatment did not affect the growth rates (Fig. 2d) or the numbers of magnetosomes per cell (transmission electron microscopy [TEM] for $n \geq 30$ cells/condition) (Fig. 2e) in wild-type MSR-1 subsequently cultured in standard FSM medium (pH 7) for 3 days (~12 to 18 generations).

**Separating magnetic WT MSR-1 from nonmagnetic Δ*mamAB* MSR-1 cells.** We demonstrate that the microfluidic technology can be applied to MSR-1, a popular model MTB strain as shown in Fig. 1b. To discriminate between different strains and to assess the performance of our device with the gold-standard fluorescence-activated cell sorting (FACS) technique, MSR-1 cells were fluorescently labeled by the constitutive expression of genetically encoded green fluorescent protein (GFP) or mCherry fluorescent protein. We minimized the flagellar motion of MSR-1 with cold/alkaline treatment before processing the samples through the magnetic microfluidic platform. Cold/alkaline treatment did not significantly affect the subsequent growth of MSR-1 wild-type (WT) and Δ*mamAB* strains (Fig. 2e; see also Fig. S3). Figure 3a shows that the MSR-1 population is distinguished from the 5-$\mu$m beads as confirmed with FACS and that most of the MSR-1 cells (~3 $\mu$m in length) were smaller than 5 $\mu$m.

Note that we continued to use a magnetic field of 373 mT for generating magnetic forces. However, throughout our experimental conditions, we found a higher isolation purity of WT MSR-1 at the selection outlet with a flow ratio of 2:1 (top medium inlet/bottom MTB inlet) with the MTB inlet flow rate maintained at 10 $\mu$l/min.

Through consultation with colleagues in the MTB field, we found that separating wild-type magnetic MTB from nonmagnetic MTB can be useful for microbiologists performing gene knockout to determine the contribution of different genes to biomineralization ability in MTB. It may also be useful as a complementary technique to characterize the magnetic properties of nonnaturally magnetic bacteria acting as a foreign expression host for the heterologous expression of magnetosome genes (10).

Figure 3b shows that wild-type (WT) MSR-1 cells were isolated at the selection outlet with 71% (WT-GFP) and 80% (WT-mCherry) efficiency, while cells of the Δ*mamAB* strain, which do not produce magnetic nanoparticles (23), were largely absent from the selection outlet. Our inability to isolate 100% of the wild-type MSR-1 cells at the selection outlet might be due to the parabolic velocity profile at the *z* axis (22) and because MSR-1 naturally produces a range of magnetosomes, even for the wild type. However, genetically modified Δ*mamAB* cells, which are nonmagnetic, were largely absent from the selection outlet, highlighting the high isolation purity of our device.

Next, we mixed equal numbers of cells (at the same optical density, 1,000 cells/$\mu$l) of WT and Δ*mamAB* MSR-1 expressing different fluorescent colors and sorted them. The isolation purity was exceptionally high, yielding ~95% of the WT populations at the selection outlet (Fig. 3c) with very minimal contamination by nonmagnetic Δ*mamAB* MSR-1. Figure 3d shows the flow cytometry results when WT-mCherry was mixed with Δ*mamAB*-GFP MSR-1. The population at the selection outlet had 93.7% purity of WT-mCherry MSR-1, while the waste outlet had 95.3% of Δ*mamAB*-GFP MSR-1. The sorted WT GFP MSR-1 also displayed similar growth and magnetosome production as the unsorted control MSR-1 (see Fig. S4).

We also applied the microfluidic system to sort another popular strain of magnetotactic bacteria, *Magnetospirillum magneticum* (AMB-1) (see conditions and rationale of experiment at Table S5). We made use of the previously generated AMB-1 mutants with

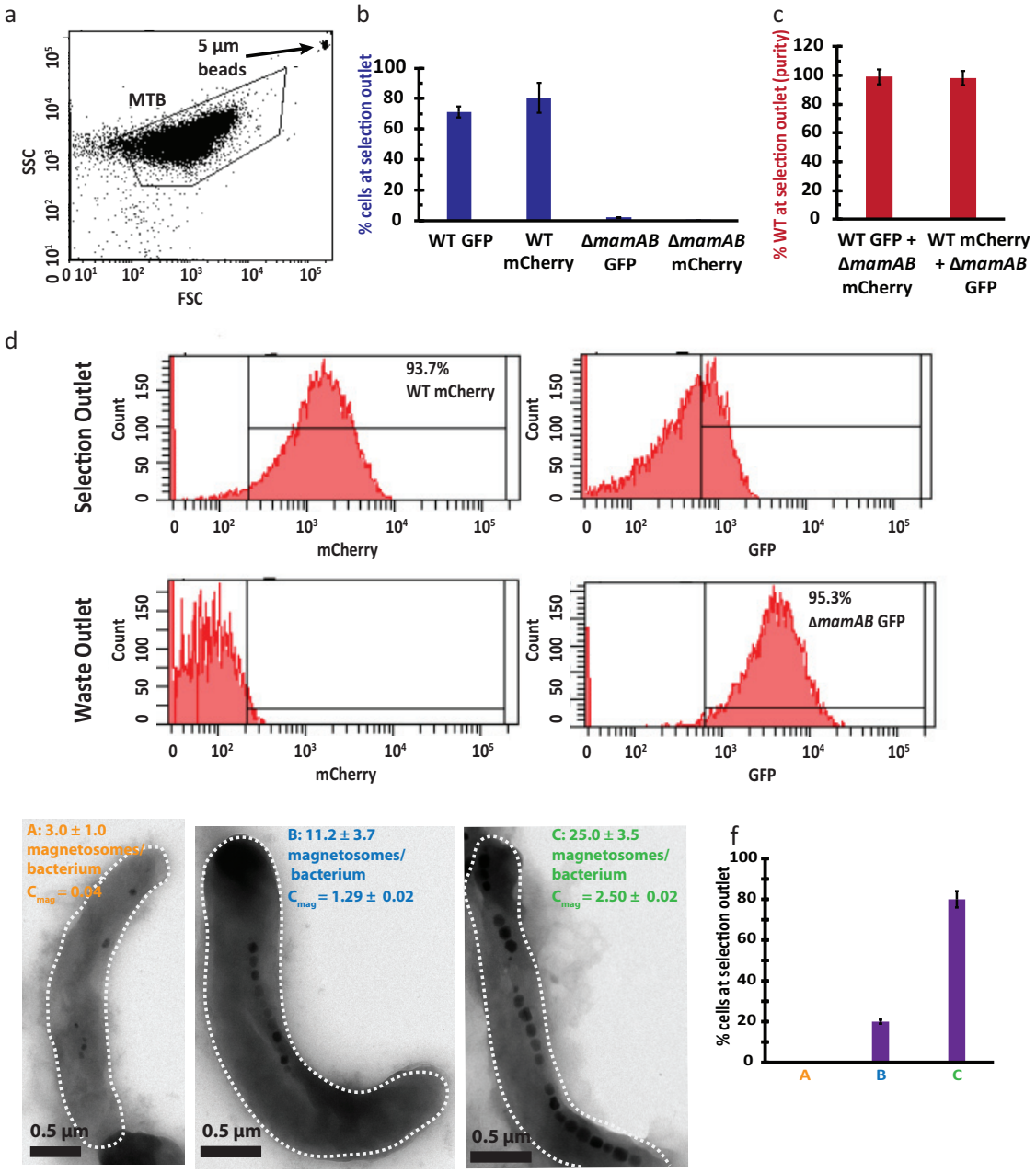


**FIG 3** Applying magnetic microfluidic device for use with MSR-1. (a) The size-based gating of MTB population can be distinguished from 5-$\mu$m beads. (b) WT magnetic MSR-1 cells were isolated from the selection outlet at high yield (~70% to 80%), while nonmagnetic Δ*mamAB* MSR-1 cells were excluded from the selection outlet. (c) The isolated cell population at the selection outlet had >95% of WT MSR-1 mixed with equal numbers of Δ*mamAB* MSR-1 (at the same optical densities, 1,000 cells/$\mu$l). (d) Example of flow cytometry showing high separation purity as the selection outlet contained 93.7% WT-mCherry MSR-1 while the waste outlet contained 95.3% Δ*mamAB*-GFP MSR-1. Note that there was some mCherry signal that was observable in the GFP channel. (e) Library of AMB-1 mutants with various numbers of magnetosomes/bacterium. Note that the scale bars are different due to use of different magnifications during imaging. (f) Experimentally obtained results of percentages of AMB-1 in different groups at the selection outlet ($n$ = 30 cells for each condition). The isolation parameters were determined such that only AMB-1 with ≥20 magnetosomes would be collected at the selection outlet; 0% of AMB-1 in group A, ~20% of AMB-1 in group B, and ~80% of AMB-1 in group C were isolated at the selection outlet. The results were close to the respective theoretical estimates of 0%, 15% and 95%. Group A, AMB-1 mutants with 0 ± 0.5 magnetosomes/bacterium; group B, AMB-1 mutants with 11.2 ± 3.7 magnetosomes/bacterium; group C, AMB-1 mutants with 25.0 ± 3.5 magnetosomes/bacterium. Error bars are standard deviations from three independent experiments.

compromised biomineralization ability with an average of 3.0 ± 0.5 magnetosomes/bacterium (group A), those with wild-type-like biomineralization ability with an average of 11.2 ± 3.7 (group B), and overproducer mutants with enhanced biomineralization ability with an average of 25.0 ± 3.5 magnetosomes/bacterium (group C) (12). Repre-

sentative cells from these populations are shown in Fig. 3e. We found previously with TEM that ~0% of cells in group A, ~15% of cells in group B, and ~95% of cells in group C have more than 20 magnetosomes/bacterium (12). Note that it is not biologically possible to obtain MTB with fixed numbers of magnetosomes/bacterium, such as 3.0, 11.0, and 25.0, as they were generated by chemical mutagenesis followed by subsequent magnetic isolation, unlike the case with the mutant Δ*mamAB* MSR-1 where the knockout of *mamAB* causes MSR-1 to lose its biomineralization ability completely. A cutoff of 20 magnetosomes/bacterium was chosen, as it was outside the normal physiological magnetosome number in wild-type AMB-1, which typically produces 11 magnetosomes. In this way, we sought to highlight the utility of our platform to isolate AMB-1 overproducers of magnetosomes that can be useful for biomedical applications, such as using MTB as biological factories for magnetosome production.

Figure 3f shows the experimentally obtained results where the locations of 30 individual AMB-1 mutants per condition (1,000 cells/$\mu$l) were tracked from image frames at the outlet captured with a high-speed camera. The results were that 0% of cells in group A, ~20% cells in group B, and ~80% of cells in group C were collected at the selection outlet. These results were close to the theoretical estimates of 0%, 15%, and 95%, respectively. The slight deviation from the theoretical estimation is due to the parabolic velocity profile in the *z* axis (22) and because AMB-1 mutants had a range of magnetosome numbers. The sorted AMB-1 also displayed similar growth and magnetosome production as the unsorted control AMB-1 (see Fig. S5).

## DISCUSSION

In this paper, we applied a simple microfluidic chip for inexpensive, high-throughput (1,000 cells/$\mu$l $\times$ 25 $\mu$l/min = 25,000 cells/min), semiautomated (only connecting the preset syringe pump to the microfluidic device was needed), and semiquantitative (threshold cutoff) estimation of magnetic content in live MTB. Semiquantification of magnetic contents in MTB can be performed by first characterizing the MTB ratio at the selection/waste outlet using MTB with known magnetosome numbers (as determined by TEM) with an established flow ratio, magnetic field strength, and flagellar inhibition conditions. The values from characterization can serve as references when researchers create new mutant strains with different magnetosome numbers and wish to characterize the efficiency of mutations or to isolate mutants with the desired mutations/cutoff magnetosome numbers.

There are a few reasons why we believe this technology can be suitably introduced and adopted by microbiology laboratories. First, the device has >20-$\mu$m dimensions, facilitating straightforward microfabrication. Second, only simple syringe pumps with preset parameters are needed to control the flow rates. Therefore, laboratories working on different MTB strains can modify the flow rates and magnetic field strengths for their specified interests, though higher flow rates may reduce the selection efficiency of MTB and require higher magnetic field gradients (14). We also acknowledge that to serve as a tool for the quantitative estimation of magnetic contents in MTB, the operating parameters of the magnetic microfluidic device must first be characterized with a known or physically similar (e.g., shape and size) MTB strain. As there is also rising interest in conferring biomineralization properties in other nonnaturally magnetic bacteria (10), our magnetic microfluidic device combined with cold/alkaline treatment strategy would be useful for the magnetic characterization of genetically modified bacteria with conferred biomineralization ability.

We also envisage a highly parallelized version of this platform to be coupled to a bioreactor for large-scale continual enrichment/selection of MTB mutants of interest (29, 30). This system would also be useful to investigate the effects of the culture environment, such as stirring, the presence of iron chelator and polyethylene glycol (PEG) (31), and genetic manipulations (11), on magnetosome production rates. These microfluidic-based applications are unique to our device, as we demonstrated the sorting of live MTB and the subsequent culturing of sorted MTB with similar proliferation and magnetosome production as the wild-type MTB. This is due to our combined

strategy of magnetic microfluidic sorting and transient cold/alkaline treatment, unlike high-heat treatment and the prolonged use of ferrofluid, which can kill MTB or have unknown long-term effects on their biology.

## MATERIALS AND METHODS

**Microfabrication.** The mold with its specific channel dimensions (length, 2 cm; width, 500 $\mu$m; height, 23 $\mu$m) was designed and fabricated using a conventional microfabrication technique (32). The microfluidic biochips were fabricated by casting a degassed polydimethylsiloxane (PDMS) polymer (mixed in a ratio of 10:1, Sylgard 184; Dow Corning, USA) on the patterned wafer and subsequently baking for 2 h at 70°C. After curing, PDMS was peeled from the patterned wafer, and access holes (0.5 mm) for fluidic inlets and outlets were punched using a Uni-Core punch (Sigma-Aldrich); then, the PDMS devices were irreversibly bonded to glass using an oxygen plasma machine (Harrick Plasma) to complete the channels. The assembled device was finally placed in an oven at 70°C for 2 h to further enhance bonding.

**Device characterization with beads.** The microfluidic devices were mounted on an inverted phase-contrast microscope coupled with a high-speed charge-coupled-device (CCD) camera (Phantom v9; Vision Research Inc., USA). The microfluidic chip was primed with buffer (1× phosphate-buffered saline [PBS], 2 mM EDTA supplemented with 0.5% bovine serum albumin [BSA]) using a syringe pump (PHD 2000; Harvard Apparatus, USA) for 2 min at a flow rate of 500 $\mu l \cdot min^{-1}$. During testing, the beads (1-$\mu$m magnetic beads to imitate MSR-1 with 20 magnetosomes and 3-$\mu$m polystyrene beads to imitate the size of MSR-1) were placed at a concentration of $1 \times 10^6$/ml into 10-ml syringes and pumped through the microfluidic device via polyether ether ketone (PEEK) tubing (0.020 in. by 1/32 in. by 5; IDEX Health & Science). Later, MTB were also sorted at this concentration. The flow rate was varied to find the optimized flow ratio, and the external magnetic field strength was also varied to optimize selection purity.

**Magnetic field measurements.** Magnets (KJ Magnetics) were set up on a Magnetic Cleanliness chamber, and the magnets were adjusted to a height such that they were aligned with the center of the Hall magnetometer sensor. The magnetic field strength was then recorded at different distances.

**Culture conditions.** All strains of MSR-1 was cultured in Hungate tubes with 2% $O_2$ in standard MSR-1 medium (FSM) (33). FSM contained (per liter deionized water) 0.1 g $KH_2PO_4$, 0.15 g $MgSO_4 \cdot 7H_2O$, 2.38 g HEPES (Biomol, Hamburg, Germany), 0.34 g $NaNO_3$, 0.1 g yeast extract (Serva, Heidelberg, Germany), 3 g soy bean peptone (Merck, Darmstadt, Germany), and 1 ml EDTA-chelated trace element mixture (34). Unless indicated otherwise, the medium contained 12 mM potassium lactate as the carbon source. Iron was added before autoclaving as ferric citrate (100 $\mu$M), and the pH of the medium was adjusted to 7.0 with NaOH. If not specified otherwise, all chemicals (analytical grade) were purchased from Fluka (Neu-Ulm, Germany). For cell sorting by length, MSR-1 WT was treated with 10°C medium at pH 8.5 for 45 min to minimize flagellar motion and was centrifuged and resuspended in normal medium before processing through the magnetic microfluidic chip. It is important to have a relatively diluted sample, as MSR-1 cells have spirillum shapes and may be clustered together, which affects the balance of the forces.

AMB-1 (ATCC 700264) was grown in magnetic *Spirillum* growth medium (MSGM) supplemented with ferric malate (30 $\mu$M), 1/100 volume of Wolfe's mineral medium (ATCC), and 1/100 volume of Wolfe's vitamin solution (ATCC), as previously described (8). The recipe for MSGM can be found online from ATCC (https://www.atcc.org/~/media/3180B81383704F779CE290819FA539EE.ashx). All ingredients in MSGM were purchased from Sigma-Aldrich. For clone selection, AMB-1 was plated on 0.7% agar supplemented with ferric malate. Cultures for $C_{mag}$ measurements or TEM were grown in 10 ml MSGM containing 25 mM HEPES buffer (pH 7.2) and ferric malate under a 10% oxygen atmosphere at 30°C. Mutagenic medium also contained 10 $\mu$g/ml 5-bromouracil. To ensure validity in comparing the isolation efficiencies of different AMB-1 mutants, the mutants were all subjected to the same growth conditions to maintain them in the exponential growth phase before processing through the microfluidic device.

**Trajectory tracking.** MSR-1 cells were tracked at room temperature using the TrackMate plugin (35) (difference of Gaussian [DoG] detector, 2.0-$\mu$m blob diameter; linking, 2 $\mu$m; filter, paths shorter than 50 frames were rejected; $\Delta t = 60$ s; $\tau = 1$ s) and an inverted fluorescence microscope (Nikon, ×20 objective). The raw data were then exported into an excel sheet for calculating the root mean square speed (RMSS) using the following formula:

$$\mathrm{RMSS} = \frac{1}{\Delta t} \times \frac{1}{p-\tau} \sum_{i=p}^{i=p-\tau} \sqrt{\left|\left(x_{i+1} - x_i\right)\right|^2 + \left|\left(y_{i+1} - y_i\right)\right|^2} \quad (1)$$

**Characterization of cellular magnetization.** The $C_{mag}$ was determined as previously described (36). Briefly, the optical density at 565 nm ($OD_{565}$) was measured with an Agilent 8000 UV-visible spectrophotometer with a magnet parallel or perpendicular to the spectrometer beam and the ratio was calculated ($C_{mag} = A_{565,perpendicular}/A_{565,parallel}$). The $C_{mag}$ measurements were performed in biological triplicates from three independently grown cultures. To ensure a fair comparison of $C_{mag}$ for the data presented in Fig. 3e, the $OD_{565}$ was kept consistent at 0.1 before $C_{mag}$ measurement.

**Characterization of growth and magnetosome production rates.** MSR-1 growth (Fig. 2d) was monitored using a plate reader (Infinite 200 Pro; Tecan). Briefly, cells were subjected to cold/alkaline (10°C/pH 8.5) treatment for 15 min to 2 h, centrifuged, diluted to the same optical densities (560 nm), and cultured in 24-well plates (Sarstedt) with normal MSR-1 medium at 28°C. Orbital shaking was performed every 5 min for 30 s with an amplitude of 6 mm, and absorbance readings were taken every

**TABLE 1** Primers used in the study

| Name | Sequence |
|---|---|
| mgr1432_for | CGGAATACCTGGAACTGTTCG |
| mgr1432_rev_pmamG | GAGCTAGTAAAGCGAAAAAGCGGGGCTTGTACGATCTAAAC |
| eGFP_rev_1434 | CGATCAGCCGGACATGATGGGGATCCTTACTTGTACAGCTC |
| mgr1434_for | CCATCATGTCCGGCTGATCG |
| mgr1434_rev | TAGCTAGCCCGGTCTGGGTCAATATGCC |
| ufpp_for | ATGGTGAGCAAGGGCGAGG |
| ufpp_rev | TTACTTGTACAGCTCGTCCATG |

20 min. Note that as the well-plate experiment was performed under an aerobic environment and MSR-1 only produced magnetosomes under microaerophilic conditions, the samples used in the growth experiment were not used for TEM. Rather, the number of magnetosomes per cell was determined by measuring the average number of magnetosomes in MSR-1 after 3 days of growth in a 15-ml capped Falcon tube with TEM (Fig. 2e; see also Fig. S4 in the supplemental material). The cell density was also estimated by the measurement of the $OD_{560}$ using an Agilent 8000 UV-visible spectrophotometer.

The growth of AMB-1 was monitored by measuring the $OD_{565}$ with an Agilent 8000 UV-visible spectrophotometer after diluting the samples to the same starting OD of 0.01. The number of magnetosomes per cell was determined by measuring the average number of magnetosomes in AMB-1 (see Fig. S5) after 3 days of growth in a 10-ml Falcon tube.

**Construction of mCherry- and GFP-labeled MSR-1 strains.** To construct fluorescence-labeled *M. gryphiswaldense* strains, a gene coding for either enhanced GFP (eGFP) or mCherry (under the control of the constitutive $P_{mamG}$ promoter) was integrated into the genome between the genes with locus tag numbers mgr_1432 and mgr_1434 of the MSR-1 wild type (37) and the nonmagnetic Δ*mamAB* strain (19) by using a previously described homologous recombination-based counterselection system (38). The construction of plasmids for homologous recombination-based integration of eGFP/mCherry-encoding genes into the genome was conducted as follows. Two PCR fragments flanking the mgr_1432-mgr_1434 intergenic region were amplified by using a proofreading DNA polymerase and primer pairs mgr1432_for/mgr1432_rev_pmamG and mgr1434_for/mgr1434_rev. Subsequently, a GFP-encoding fragment (harboring also the $P_{mamG}$ promoter) was fused between both PCR fragments via two rounds of overlap extension PCR, employing both fragments and pAP150 (39) as the templates. The primer pairs mgr1432_for/eGFP_rev_1434 and mgr1432_for/mgr1434_rev were used for the first and second rounds of the overlap extension PCR, respectively. The final fragment was then subcloned into pJET, cut with XhoI/NheI, and ligated into a XhoI/NheI-digested pORFM-galK vector (37). The construction of the mCherry insertion vector was conducted the same way by exchanging GFP for mCherry (amplified with primers ufpp_for and ufpp_rev) in the pJET vector according to the mega-primer method of Bryksin and Matsumura (40). Refer to Fig. S6 for a graphical illustration. The primers used are shown in Table 1.

**Microscopy.** MSR-1 was isolated according to the experimental conditions stated in Table S5. The samples were then centrifuged at 14,000 rpm for 10 min, followed by resuspension in the leftover medium. Liquid agarose (1% [wt/vol], 700 $\mu$l) was pipetted onto a glass slide and allowed to gel for 30 min. Five microliters of the sample suspension was then pipetted onto the agarose pad before differential interference contrast (DIC) imaging with an Olympus IX81 microscope (×100 objective).

**Electron microscopy.** An aliquot of cell culture (100 to 500 $\mu$l) was pelleted by a brief centrifugation (14,000 × *g*) for 10 min aerobically at room temperature and resuspended in MSGM (~10 $\mu$l). The cells were adsorbed onto a 400-mesh copper grid coated with Formvar/Carbon (Ted Pella Inc.). TEM was performed using 120-kV T12 Quick CryoEM with a point resolution of 0.34 nm. Imaging and data processing were performed at the University of California, Los Angeles, California Nanosystems Institute (UCLA CNSI) Electron Imaging Center for NanoMachines (EICN).

**Statistical analysis.** Statistical analyses of the mean square speeds of MSR-1/AMB-1 cells at different temperatures (Fig. 2b), pHs (Fig. 2c) ($n = 25$ for each condition), and magnetosome numbers ($n \geq 30$ cells/condition) (Fig. 2e) were performed using Student's *t* tests after testing for normality by plotting the data as a bell-shaped histogram.

## SUPPLEMENTAL MATERIAL

Supplemental material for this article may be found at https://doi.org/10.1128/AEM.01308-18.

**SUPPLEMENTAL FILE 1,** PDF file, 0.5 MB.

**SUPPLEMENTAL FILE 2,** MOV file, 13.1 MB.

## ACKNOWLEDGMENTS

This work was funded by the U.S. National Institutes of Health Director's New Innovator Award (1DP2OD007113) and a Bavaria-California Technology Center grant.

Chip fabrication was performed at the CNSI Center for Micro- and Nanofabrication and Advanced Light Microscopy/Spectroscopy Shared Resource Facility at UCLA supported with funding from an NIH-NCRR shared resources grant (CJX1-443835-WS-

29646) and NSF Major Research Instrumentation grant (CHE-0722519), respectively. We acknowledge the use of instruments at the Electron Imaging Center for NanoMachines supported by the NIH (1S10RR23057 to Z. Hong Zhou).

We thank Keegan Owsley for his help on microfluidic platform design, Harsha Kittur for measuring the height of the silicon wafers, Stephan Förster and Mathias Schlenk at the University of Bayreuth for kindly providing syringe pumps, and Agata Käsbohrer for help with the construction of fluorescently labeled MSR-1 strains.

A. Tay designed the study, performed all experiments (microfluidic flow characterization, trajectory tracking, flow cytometry, and MTB culture) and analyzed data. D. Pfeiffer, F. Popp, and D. Schüler provided MSR-1 samples and data on MSR-1 growth after cold/alkaline treatments. A. Tay, K. Rowe, A. Tannenbaum, and R. Strangeway measured the magnetic field decay. A. Tay wrote the manuscript, D. Pfeiffer helped greatly in revision, and all authors revised the manuscript.

## REFERENCES

1. Wu W, Wu Z, Yu T, Jiang C, Kim W-S. 2015. Recent progress on magnetic iron oxide nanoparticles: synthesis, surface functional strategies and biomedical applications. Sci Technol Adv Mater 16:023501. https://doi.org/10.1088/1468-6996/16/2/023501.
2. Tay A, Schweizer FE, Di Carlo D. 2016. Micro- and nano-technologies to probe the mechano-biology of the brain. Lab Chip 16:1962–1977. https://doi.org/10.1039/C6LC00349D.
3. Yan L, Zhang S, Chen P, Liu H, Yin H, Li H. 2012. Magnetotactic bacteria, magnetosomes and their application. Microbiol Res 167:507–519. https://doi.org/10.1016/j.micres.2012.04.002.
4. Valencia PM, Farokhzad OC, Karnik R, Langer R. 2012. Microfluidic technologies for accelerating the clinical translation of nanoparticles. Nat Nanotechnol 7:623–629. https://doi.org/10.1038/nnano.2012.168.
5. Pollithy A, Romer T, Lang C, Müller FD, Helma J, Leonhardt H, Rothbauer U, Schüler D. 2011. Magnetosome expression of functional camelid antibody fragments (nanobodies) in *Magnetospirillum gryphiswaldense*. Appl Environ Microbiol 77:6165–6171. https://doi.org/10.1128/AEM.05282-11.
6. Di Corato R, Espinosa A, Lartigue L, Tharaud M, Chat S, Pellegrino T, Ménager C, Gazeau F, Wilhelm C. 2014. Magnetic hyperthermia efficiency in the cellular environment for different nanoparticle designs. Biomaterials 35:6400–6411. https://doi.org/10.1016/j.biomaterials.2014.04.036.
7. Lee J-H, Jang J-T, Choi J-S, Moon SH, Noh S-H, Kim J-W, Kim J-G, Kim I-S, Park KI, Cheon J. 2011. Exchange-coupled magnetic nanoparticles for efficient heat induction. Nat Nanotechnol 6:418–422. https://doi.org/10.1038/nnano.2011.95.
8. Jones SR, Wilson TD, Brown ME, Rahn-Lee L, Yu Y, Fredriksen LL, Ozyamak E, Komeili A, Chang MCY. 2015. Genetic and biochemical investigations of the role of MamP in redox control of iron biomineralization in *Magnetospirillum magneticum*. Proc Natl Acad Sci U S A 112:3904–3909. https://doi.org/10.1073/pnas.1417614112.
9. Prozorov T, Bazylinski DA, Mallapragada SK, Prozorov R. 2013. Novel magnetic nanomaterials inspired by magnetotactic bacteria: topical review. Mater Sci Eng R Rep 74:133–172. https://doi.org/10.1016/j.mser.2013.04.002.
10. Kolinko I, Lohße A, Borg S, Raschdorf O, Jogler C, Tu Q, Pósfai M, Tompa E, Plitzko JM, Brachmann A, Wanner G, Müller R, Zhang Y, Schüler D. 2014. Biosynthesis of magnetic nanostructures in a foreign organism by transfer of bacterial magnetosome gene clusters. Nat Nanotechnol 9:193–197. https://doi.org/10.1038/nnano.2014.13.
11. Lohße A, Kolinko I, Raschdorf O, Uebe R, Borg S, Brachmann A, Plitzko JM, Müller R, Zhang Y, Schüler D. 2016. Overproduction of magnetosomes by genomic amplification of biosynthetic gene clusters in a magnetotactic bacterium. Appl Environ Microbiol 82:3032–3041. https://doi.org/10.1128/AEM.03860-15.
12. Tay A, Murray C, Di Carlo D. 2017. Phenotypic selection of *Magnetospirillum magneticum* (AMB-1) overproducers using magnetic ratcheting. Adv Funct Mater 27:1703106. https://doi.org/10.1002/adfm.201703106.
13. Schultheiss D, Schüler D. 2003. Development of a genetic system for *Magnetospirillum gryphiswaldense*. Arch Microbiol 179:89–94. https://doi.org/10.1007/s00203-002-0498-z.
14. Myklatun A, Cappetta M, Winklhofer M, Ntziachristos V, Westmeyer GG. 2017. Microfluidic sorting of intrinsically magnetic cells under visual control. Sci Rep 7:6942. https://doi.org/10.1038/s41598-017-06946-x.
15. Gossett DR, Weaver WM, MacH AJ, Hur SC, Tse HTK, Lee W, Amini H, Di Carlo D. 2010. Label-free cell separation and sorting in microfluidic systems. Anal Bioanal Chem 397:3249–3267. https://doi.org/10.1007/s00216-010-3721-9.
16. Xia N, Hunt TP, Mayers BT, Alsberg E, Whitesides GM, Westervelt RM, Ingber DE. 2006. Combined microfluidic-micromagnetic separation of living cells in continuous flow. Biomed Microdevices 8:299–308. https://doi.org/10.1007/s10544-006-0033-0.
17. Tay A, Pavesi A, Yazdi SR, Lim CT, Warkiani ME. 2016. Advances in microfluidics in combating infectious diseases. Biotechnol Adv 34:404–421. https://doi.org/10.1016/j.biotechadv.2016.02.002.
18. Schultheiss D, Kube M, Schüler D. 2004. Inactivation of the flagellin gene flaA in *Magnetospirillum gryphiswaldense* results in nonmagnetotactic mutants lacking flagellar filaments. Appl Environ Microbiol 70:3624–3631. https://doi.org/10.1128/AEM.70.6.3624-3631.2004.
19. Ullrich S, Schüler D. 2010. Cre-lox-based method for generation of large deletions within the genomic magnetosome island of *Magnetospirillum gryphiswaldense*. Appl Environ Microbiol 76:2439–2444. https://doi.org/10.1128/AEM.02805-09.
20. Leith D. 1987. Drag on nonspherical objects. Aerosol Sci Technol 6:153–161. https://doi.org/10.1080/02786828708959128.
21. Kong D, Lin W, Pan Y, Zhang K. 2014. Swimming motion of rod-shaped magnetotactic bacteria: The effects of shape and growing magnetic moment. Front Microbiol 5:8. https://doi.org/10.3389/fmicb.2014.00008.
22. Di Carlo D. 2009. Inertial microfluidics. Lab Chip 9:3038. https://doi.org/10.1039/b912547g.
23. Uebe R, Schüler D. 2016. Magnetosome biogenesis in magnetotactic bacteria. Nat Rev Microbiol 14:621–637. https://doi.org/10.1038/nrmicro.2016.99.
24. Zondervan L, Sukas ÖS, Khalil ISM, Pichel MP, Misra S, Abelmann L. 2014. Magnetic torque of microfabricated elements and magnetotactic bacteria. Class Phys arXiv:1408.1570. https://arxiv.org/abs/1408.1570v1.
25. Lefèvre CT, Bennet M, Landau L, Vach P, Pignol D, Bazylinski DA, Frankel RB, Klumpp S, Faivre D. 2014. Diversity of magneto-aerotactic behaviors and oxygen sensing mechanisms in cultured magnetotactic bacteria. Biophys J 107:527–538. https://doi.org/10.1016/j.bpj.2014.05.043.
26. Li Y, Sabaty M, Borg S, Silva KT, Pignol D, Schüler D. 2014. The oxygen sensor MgFnr controls magnetite biomineralization by regulation of denitrification in *Magnetospirillum gryphiswaldense*. BMC Microbiol 14:153. https://doi.org/10.1186/1471-2180-14-153.
27. Popp F, Armitage JP, Schüler D. 2014. Polarity of bacterial magnetotaxis is controlled by aerotaxis through a common sensory pathway. Nat Commun 5:5398. https://doi.org/10.1038/ncomms6398.
28. Maurer LM, Yohannes E, Bondurant SS, Radmacher M, Slonczewski JL. 2005. pH regulates genes for flagellar motility, catabolism, and oxidative stress in *Escherichia coli* K-12. J Bacteriol 187:304–319. https://doi.org/10.1128/JB.187.1.304-319.2005.
29. Warkiani ME, Tay AKP, Guan G, Han J. 2015. Membrane-less microfiltration using inertial microfluidics. Sci Rep 5:11018. https://doi.org/10.1038/srep11018.
30. Tay AKP. 2018. Magnetic microfluidic separation for estimating the

magnetic contents of magnetotactic bacteria, p 71–81. *In* Acute and chronic neural stimulation via mechano-sensitive ion channels. Springer theses. Springer, Cham, Switzerland.
31. Shimoshige H, Kobayashi H, Mizuki T, Nagaoka Y, Inoue A, Maekawa T. 2015. Effect of polyethylene glycol on the formation of magnetic nanoparticles synthesized by *Magnetospirillum magnetotacticum* MS-1. PLoS One 10:e0127481. https://doi.org/10.1371/journal.pone.0127481.
32. Warkiani ME, Tay AKP, Khoo BL, Xiaofeng X, Han J, Lim CT. 2015. Malaria detection using inertial microfluidics. Lab Chip 15:1101–1109. https://doi.org/10.1039/C4LC01058B.
33. Heyen U, Schüler D. 2003. Growth and magnetosome formation by microaerophilic *Magnetospirillum* strains in an oxygen-controlled fermentor. Appl Microbiol Biotechnol 61:536–544. https://doi.org/10.1007/s00253-002-1219-x.
34. Widdel F, Bak F. 1992. Gram-negative mesophilic sulfate-reducing bacteria, p 3352–3378. *In* Balows A, Trüper HG, Dworkin M, Harder W, Schleifer KH (ed), The prokaryotes. Springer, New York, NY.
35. Jaqaman K, Loerke D, Mettlen M, Kuwata H, Grinstein S, Schmid SL, Danuser G. 2008. Robust single-particle tracking in live-cell time-lapse sequences. Nat Methods 5:695–702. https://doi.org/10.1038/nmeth.1237.
36. Zhao L, Wu D, Wu L-F, Song T. 2007. A simple and accurate method for quantification of magnetosomes in magnetotactic bacteria by common spectrophotometer. J Biochem Biophys Methods 70:377–383. https://doi.org/10.1016/j.jbbm.2006.08.010.
37. Schleifer KH, Schüler D, Spring S, Weizenegger M, Amann R, Ludwig W, Köhler M. 1991. The genus *Magnetospirillum* gen. nov. Description of *Magnetospirillum gryphiswaldense* sp. nov. and transfer of *Aquaspirillum magnetotacticum* to *Magnetospirillum magnetotacticum* comb. Nov. Syst Appl Microbiol 14:379–385. https://doi.org/10.1016/S0723-2020(11)80313-9.
38. Raschdorf O, Plitzko JM, Schüler D, Müller FD. 2014. A tailored galK counterselection system for efficient markerless gene deletion and chromosomal tagging in *Magnetospirillum gryphiswaldense*. Appl Environ Microbiol 80:4323–4330. https://doi.org/10.1128/AEM.00588-14.
39. Borg S, Hofmann J, Pollithy A, Lang C, Schüler D. 2014. New vectors for chromosomal integration enable high-level constitutive or inducible magnetosome expression of fusion proteins in *Magnetospirillum gryphiswaldense*. Appl Environ Microbiol 80:2609–2616. https://doi.org/10.1128/AEM.00192-14.
40. Bryksin AV, Matsumura I. 2010. Overlap extension PCR cloning: a simple and reliable way to create recombinant plasmids. Biotechniques 48:463–465. https://doi.org/10.2144/000113418.